

# Unreal is all you need: Multimodal ISAC Data Simulation with Only One Engine

Kongwu Huang<sup>\*1</sup> Shiyi Mu<sup>\*1</sup> Jun Jiang<sup>\*1</sup> Yuan Gao<sup>1</sup> Shugong Xu<sup>†2</sup>

<sup>1</sup>Shanghai University, Shanghai, China

<sup>2</sup>Xi'an Jiaotong-Liverpool University, Suzhou, China

{huangkongwu, shiyimu, jun\_jiang, gaoyuansie}@shu.edu.cn

shugong.xu@xjtlu.edu.cn

<sup>1</sup> \*These authors contributed equally to this work. <sup>†</sup>Corresponding author.

**Abstract**—Scaling laws have achieved success in LLM and foundation models. To explore their potential in ISAC research, we propose Great-X. This single-engine multimodal data twin platform reconstructs the ray-tracing computation of Sionna within Unreal Engine and is deeply integrated with autonomous driving tools. This enables efficient and synchronized simulation of multimodal data, including CSI, RGB, Radar, and LiDAR. Based on this platform, we construct an open-source, large-scale, low-altitude UAV multimodal synaesthesia dataset named Great-MSD, and propose a baseline CSI-based UAV 3D localization algorithm, demonstrating its feasibility and generalizability across different CSI simulation engines. The related code and dataset will be made available at: <https://github.com/hkw-xg/Great-MCD>.

**Index Terms**—Multimodal ISAC Simulator, Ray Tracing, 6G

## I. INTRODUCTION

The synergy between communication and multimodal perception is a key feature of the future 6G and subsequent wireless systems. Such systems are expected to achieve communication and perception functions simultaneously, or to utilize one function to enhance the other [1]. Therefore, this integration has catalyzed several emerging research directions, including multimodal perception-assisted communication and integrated perception and communication (ISAC) [2]–[4]. In the context of 6G, data-driven deep learning methods have great potential; however, their development and evaluation largely depend on the availability of large-scale, high-quality datasets [5]. Although progress has been made recently, there is still a lack of open-source multimodal simulation platforms that can generate large-scale data in multiple scenarios, especially in low-altitude unmanned aerial vehicle (UAV) scenarios. Moreover, a unified multimodal data benchmark covering standardized evaluation metrics has not yet been established.

Given the challenges above, there is an urgent need for an open, flexible, and unified simulation framework that can support the joint modeling and evaluation of communication and multimodal perception functions within a single engine architecture. To address this issue, we have proposed Great-X - an open-source simulation platform designed explicitly for 6G multimodal ISAC research. This platform is built based on the Unreal Engine (UE) and adopts a single-engine architecture.



(a) Realistic 3D UAV models in Great-X.



(b) Lujiazui simulation scene in Shanghai.

Fig. 1: Overview of the Great-X simulator, showcasing realistic UAV models and urban environments (The green lines represent the emission path of the light, the white line indicates the scattering path, and the red denotes the reflection path.).

Based on the Ray-tracing channel modeling method, it can simultaneously generate RF data (such as CSI and millimeter-wave radar echoes). As shown in Figure 1, the simulated scenario of this platform depicts the process of a UAV performing low-altitude flight missions in the Lujiazui area of Shanghai, and its communication and perception interaction with ground base stations.

Among the existing solutions, commercial ray-tracing software such as Wireless InSite (WI) has been widely adopted to simulate channel state information (CSI). Although these tools offer accurate electromagnetic propagation modeling,

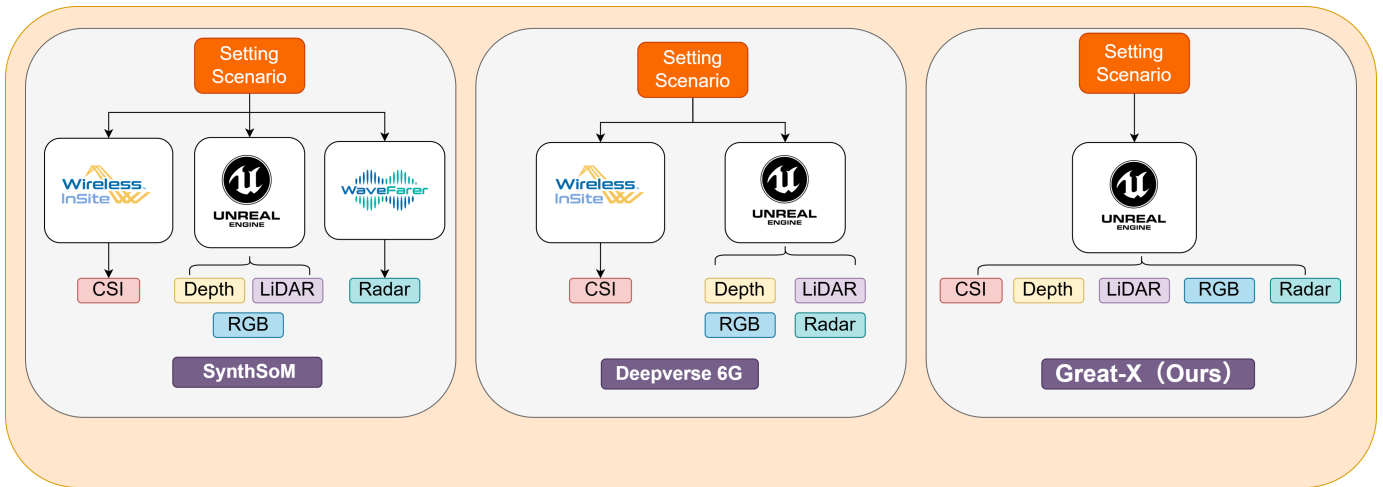


Fig. 2: Comparing Great-X and DeepVerse 6G, the data generation of SynthSoM.

they often lack flexibility, scalability, and openness, which are key requirements for advancing data-driven methodologies in 6G systems.

For instance, the well-known DeepMIMO [6] is built upon WI [7]-based simulations. Although it is a valuable resource for studying AI-enabled wireless communication in predefined scenarios, it lacks support for user-defined scene configurations. It is limited to single-modality communication data, with no native integration of multimodal perception signals.

As shown in Fig 2, recent efforts have attempted to bridge this gap by incorporating perception modalities into ISAC simulators. One notable example is DeepVerse 6G [8], which extends DeepMIMO by integrating multimodal perception data such as images and LiDAR through a co-simulation framework combining WI and the CARLA [9] autonomous driving simulator. Despite its enhanced functionality, DeepVerse 6G remains closed-source, limiting its reproducibility and broader adoption within the research community. Furthermore, its dual-engine architecture introduces system complexity and restricts real-time synchronization.

Another related work, SynthSoM [10], couples Wireless InSite and WaveFarer [11] with AirSim [12] to generate multimodal sensory data, including images, radar, LiDAR point clouds, and CSI. While supporting multiple perception modalities, it follows a multi-engine heterogeneous simulation paradigm, where communication modeling still depends on the commercial engine. Consequently, it inherits similar limitations regarding open access, extensibility, and cost-effectiveness.

To address the challenges above, we propose a new open-source multimodal communication dataset, Great-MSD, and a unified simulation platform, Great-X. Together, they provide an integrated environment for generating and evaluating multimodal data in representative 6G scenarios. The key contributions and innovations of this work are summarized as follows:

1) We have developed the first unified open-source sim-

ulation platform, Great-X, for multimodal perception, enabling synchronous optical and channel simulation for a single engine.

- 2) We used Unreal Engine to reconstruct the electromagnetic process of channel simulation based on ray tracing, thereby improving the simulation speed.
- 3) Based on GREAT-X, we have developed a multimodal UAV detection simulation dataset named Great-MSD for low-altitude scenarios, which includes camera data, channel data, and accurate spatial coordinate data.
- 4) The relevant datasets and demo Code will be made open source.

Our work establishes Great-X as a foundational framework for 6G ISAC research by simultaneously addressing the triad of openness, scalability, and fidelity in multimodal simulations. The release of Great-MSD further provides a standardized benchmark for evaluating emerging algorithms in dynamic aerial environments, advancing the field toward reproducible and extensible research methodologies.

## II. THE GREAT-X: ALL-IN-UE MULTIMODAL SIMULATOR

The constructed simulation platform reconstructs the electromagnetic process of the ray tracing channel simulation in the Unreal Engine, thereby enabling the implementation of the ray tracing algorithm based on ray tracing in high-fidelity scenarios. The following mainly introduces the reflection, refraction, and the scattering parts. The following formulas are referenced from SionnaRT [13].

During the propagation of electromagnetic waves, when a plane wave is incident on the planar interface between two different media, due to the difference in medium properties, part of the wave will be reflected at the interface, while the other part will pass through the interface and enter the second medium; that is, transmission or refraction occurs. For analysis, this paper assumes that both media are uniform and non-magnetic dielectrics and adopts the parameter definitions in ITU recommendations [14]. The complex amplitude vector

of the incident wave's electric field,  $\mathbf{E}_i$ , can be represented by two arbitrary orthogonal polarization components:

$$\mathbf{E}_i = E_{i,s} \hat{\mathbf{e}}_{i,s} + E_{i,p} \hat{\mathbf{e}}_{i,p} \quad (1)$$

Fig 3 illustrates the reflection and refraction phenomena that occur when electromagnetic waves are incident on a planar interface between two materials with relative dielectric constants of  $\eta_1$  and  $\eta_2$ . For ease of analysis, the coordinate system is chosen such that the wave vectors of the incident wave, reflected wave, and transmitted wave are all located in the same incident plane, which is defined as the  $x$ - $z$  plane. At the same time, the normal vector  $\hat{\mathbf{n}}$  of the interface is oriented along the negative  $z$  axis. Due to the different polarization characteristics, the incident wave needs to be expanded in a set of specific bases, specifically expressed as two mutually orthogonal polarization components  $E_{i,\perp}$  and  $E_{i,\parallel}$ , that is:

$$\mathbf{E}_i = E_{i,\perp} \hat{\mathbf{e}}_{i,\perp} + E_{i,\parallel} \hat{\mathbf{e}}_{i,\parallel} \quad (2)$$

Among them, the component perpendicular to the incident plane is called transverse electric (TE) polarization (on the left side of the figure). In contrast, the component parallel to the incident plane is called transverse magnetic (TM) polarization (on the right side of the figure). In the subsequent discussion, it is uniformly agreed that all the transverse vector components point outward from the plane of the figure. Based on the above definition, it can be directly verified that the following relationships must be satisfied:

$$\hat{\mathbf{e}}_{i,\perp} = \frac{\hat{\mathbf{k}}_i \times \hat{\mathbf{n}}}{\|\hat{\mathbf{k}}_i \times \hat{\mathbf{n}}\|}, \hat{\mathbf{e}}_{i,\parallel} = \hat{\mathbf{e}}_{i,\perp} \times \hat{\mathbf{k}}_i \quad (3)$$

The incident electric field phasor in terms of its TE and TM components can be expressed as:

$$\begin{aligned} \begin{bmatrix} E_{i,\perp} \\ E_{i,\parallel} \end{bmatrix} &= \begin{bmatrix} \hat{\mathbf{e}}_{i,\perp}^\top \hat{\mathbf{e}}_{i,s} & \hat{\mathbf{e}}_{i,\perp}^\top \hat{\mathbf{e}}_{i,p} \\ \hat{\mathbf{e}}_{i,\parallel}^\top \hat{\mathbf{e}}_{i,s} & \hat{\mathbf{e}}_{i,\parallel}^\top \hat{\mathbf{e}}_{i,p} \end{bmatrix} \begin{bmatrix} E_{i,s} \\ E_{i,p} \end{bmatrix} \\ &= \mathbf{W}(\hat{\mathbf{e}}_{i,\perp}, \hat{\mathbf{e}}_{i,\parallel}, \hat{\mathbf{e}}_{i,s}, \hat{\mathbf{e}}_{i,p}) \begin{bmatrix} E_{i,s} \\ E_{i,p} \end{bmatrix} \end{aligned} \quad (4)$$

The phasors of the reflected wave and the transmitted wave  $\mathbf{E}_r$  and  $\mathbf{E}_t$  are also expressed in a similar manner:

$$\begin{aligned} \mathbf{E}_r &= E_{r,\perp} \hat{\mathbf{e}}_{r,\perp} + E_{r,\parallel} \hat{\mathbf{e}}_{r,\parallel}, \\ \mathbf{E}_t &= E_{t,\perp} \hat{\mathbf{e}}_{t,\perp} + E_{t,\parallel} \hat{\mathbf{e}}_{t,\parallel}. \end{aligned} \quad (5)$$

The corresponding unit vectors for the reflected and transmitted waves are defined as follows:

$$\begin{aligned} \hat{\mathbf{e}}_{r,\perp} &= \hat{\mathbf{e}}_{i,\perp}, \hat{\mathbf{e}}_{r,\parallel} = \frac{\hat{\mathbf{e}}_{r,\perp} \times \hat{\mathbf{k}}_r}{\|\hat{\mathbf{e}}_{r,\perp} \times \hat{\mathbf{k}}_r\|}, \\ \hat{\mathbf{e}}_{t,\perp} &= \hat{\mathbf{e}}_{i,\perp}, \hat{\mathbf{e}}_{t,\parallel} = \frac{\hat{\mathbf{e}}_{t,\perp} \times \hat{\mathbf{k}}_t}{\|\hat{\mathbf{e}}_{t,\perp} \times \hat{\mathbf{k}}_t\|}. \end{aligned} \quad (6)$$

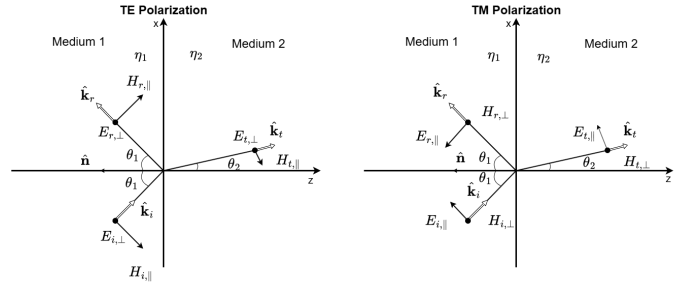


Fig. 3: Reflection and refraction of a plane wave at a plane interface between two materials [13].

Combining all the information, we obtain the following relationship among the incident wave, the reflected wave, and the transmitted wave:

$$\begin{bmatrix} E_{r,\perp} \\ E_{r,\parallel} \end{bmatrix} = \begin{bmatrix} r_{\perp} & 0 \\ 0 & r_{\parallel} \end{bmatrix} \mathbf{W}(\hat{\mathbf{e}}_{i,\perp}, \hat{\mathbf{e}}_{i,\parallel}, \hat{\mathbf{e}}_{i,s}, \hat{\mathbf{e}}_{i,p}) \begin{bmatrix} E_{i,s} \\ E_{i,p} \end{bmatrix}, \quad (7a)$$

$$\begin{bmatrix} E_{t,\perp} \\ E_{t,\parallel} \end{bmatrix} = \begin{bmatrix} t_{\perp} & 0 \\ 0 & t_{\parallel} \end{bmatrix} \mathbf{W}(\hat{\mathbf{e}}_{i,\perp}, \hat{\mathbf{e}}_{i,\parallel}, \hat{\mathbf{e}}_{i,s}, \hat{\mathbf{e}}_{i,p}) \begin{bmatrix} E_{i,s} \\ E_{i,p} \end{bmatrix}. \quad (7b)$$

In the phenomenon of scattering, when an electromagnetic wave is incident on a surface, some of the energy is reflected. At the same time, the other part penetrates the surface and enters the medium interior, forming a refracted wave. We usually classify reflection into two types: specular reflection and diffuse reflection. The former has been analyzed in the discussion of reflection and refraction, while this section will focus on the latter, namely diffuse reflection. Unlike specular reflection, when an electromagnetic wave is incident on a surface with diffuse reflection properties, the energy does not concentrate and reflect in a single direction, but is scattered in multiple directions outward. Considering that most actual surfaces will simultaneously produce specular reflection and diffuse reflection, we use  $S^2$  to represent the energy of the diffuse reflection part, where  $S \in [0, 1]$  is the scattering coefficient; correspondingly,  $R^2$  represents the energy of the specular reflection part, where  $R \in [0, 1]$  is the specular reflection attenuation factor. The relationship between the two is as follows:

$$R = \sqrt{1 - S^2} \quad (8)$$

Consider the scenario depicted in Fig 4, where at the scattering point  $\mathbf{q}$ , there exists a plane incident wave with local linear polarization, and its electric field vector is  $\mathbf{E}_i(\mathbf{q})$ . Our focus is on the scattered field generated by this incident wave on the scattering direction  $\hat{\mathbf{k}}_s$ , through an infinitesimal surface element  $dA$ . It should be noted that the surface normal vector  $\hat{\mathbf{n}}$  is in any direction in the global coordinate system, and the  $(x, y, z)$  coordinate axes indicated by the green dotted lines in the figure are used to assist in the explanation. The incident field vector can be expressed as two orthogonal polarization components perpendicular to the incident wave direction  $\hat{\mathbf{k}}_i$ :

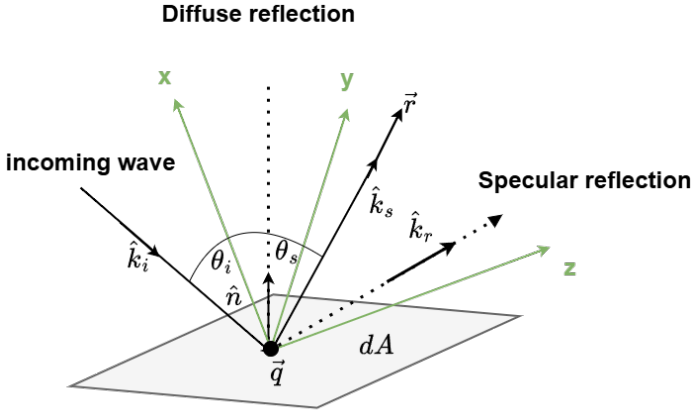


Fig. 4: Diffuse and specular reflection of an incoming wave [13].

The incident electric field phasor  $\mathbf{E}_i(\mathbf{q})$  can be expressed in different polarization or angular bases as follows:

$$\begin{aligned} \mathbf{E}_i(\mathbf{q}) &= E_{i,s}\hat{\mathbf{e}}_{i,s} + E_{i,p}\hat{\mathbf{e}}_{i,p} \\ &= E_{i,\perp}\hat{\mathbf{e}}_{i,\perp} + E_{i,\parallel}\hat{\mathbf{e}}_{i,\parallel} \\ &= E_{i,\theta}\hat{\boldsymbol{\theta}}(\hat{\mathbf{k}}_i) + E_{i,\varphi}\hat{\boldsymbol{\varphi}}(\hat{\mathbf{k}}_i) \end{aligned} \quad (9)$$

The diffuse scattering field  $\mathbf{E}_s(\mathbf{r})$  at the observation point  $\mathbf{r}$  is modeled as:

$$\mathbf{E}_s(\mathbf{r}) = E_{s,\theta}\hat{\boldsymbol{\theta}}(\hat{\mathbf{k}}_s) + E_{s,\varphi}\hat{\boldsymbol{\varphi}}(\hat{\mathbf{k}}_s) \quad (10)$$

The orthogonal field components are calculated using the following relation:

$$\begin{bmatrix} E_{s,\theta} \\ E_{s,\varphi} \end{bmatrix} = \frac{ST}{\|\mathbf{r}-\mathbf{q}\|} \sqrt{f_s(\hat{\mathbf{k}}_i, \hat{\mathbf{k}}_s, \hat{\mathbf{n}}) \cos \theta_i dA} \cdot \begin{bmatrix} \sqrt{1-K_x} e^{j\chi_1} \\ \sqrt{K_x} e^{j\chi_2} \end{bmatrix} \cdot \begin{bmatrix} E_{i,\theta} \\ E_{i,\varphi} \end{bmatrix} \quad (11)$$

Here,  $\Gamma^2$  represents the percentage of reflected (by the mirror and diffuse) power in the incident power, and it can be calculated as

$$\Gamma = \frac{\sqrt{|r_{\perp}E_{i,\perp}|^2 + |r_{\parallel}E_{i,\parallel}|^2}}{\|\mathbf{E}_i(\mathbf{q})\|} \quad (12)$$

The above processes were implemented based on the Unreal Engine [15] and C++ code refactoring.

### III. THE GREAT-MSD: MULTIMODAL DATASET

Based on the aforementioned ray tracing-based channel simulation methodology, we utilized the Great-X to import a 3D model of a UAV, simulate its flight trajectory, and record multimodal data including CSI, RGB images, depth maps, and positional metadata. Through this process, we constructed the Great-MSD dataset, a large-scale multimodal dataset for low-altitude communication scenarios.

As illustrated in Fig 5, in the Great-MSD dataset, the UAV takes off from a distant location and gradually approaches the base station along a predefined trajectory. During the flight,

TABLE I: Key configuration for the Great-MSD.

Parameter	Value
Camera Field of View (angle)	90°
Camera & BS Position(m)	[57.70, 0.01, 25.70]
Camera Rotation	[10,170,0]
BS Rotation	[0,0,0]
Transmitting Antenna Array Structure	4x8 UPA, Cross-polarized
Transmitting Antenna Placement	yz-plane
Vertical Element Spacing (Transmitter)	2.0 units
Horizontal Element Spacing (Transmitter)	0.5 units
Receiving Antenna Structure	1x1
Element Spacing (Receiver)	0.5 units

multimodal data are recorded frame by frame, effectively capturing the dynamic evolution of the channel environment with varying distances. This design also provides rich and diverse samples to support downstream tasks such as channel modeling, target detection, and localization.

We randomly generated 100 distinct flight paths within a three-dimensional space measuring 170 meters in length, 16 meters in width, and 30 meters in height. Each trajectory was flown at a constant speed of 1 m/s, with 1000 sampling points collected per path. Of these, 90 trajectories were allocated to the training set, while the remaining 10 were reserved for testing, ensuring a robust evaluation framework for learning-based models.

Key configuration parameters of the simulation setup are summarized in Table I for clarity and reproducibility.

### IV. EXPERIMENTS

We design a simple 3D positioning experiment with CSI in ResNet-50 [16].

Fig 6 demonstrates that as the number of training trajectories increases, the average positioning error gradually decreases, indicating that the model is learning increasingly robust feature representations. Specifically, when the number of training trajectories increases from 20 to 90, the average positioning error drops from 8.53 meters to 4.95 meters, showing a significant performance improvement. More importantly, the diminishing error reduction rate suggests that the model is approaching convergence.

This trend not only highlights the dataset's good convergence properties but also illustrates its scalability potential with increasing data volume. It indicates that our dataset supports effective learning even under larger-scale settings, enabling the development of even larger datasets in the future for broader applicability.

To assess the effectiveness of the simulation platform, we conducted a bidirectional cross-platform evaluation between Great-X and SionnaRT. Both platforms used identical map configurations and consistent parameters.

As shown in Table II, the model trained on the Great-MSD exhibits strong cross-platform generalization capabilities. When evaluated on 10 unseen test trajectories generated by the SionnaRT, it achieves an average positioning error of 8.107 meters, which remains relatively low despite the domain shift. Conversely, the model trained using the Sionna RT shows



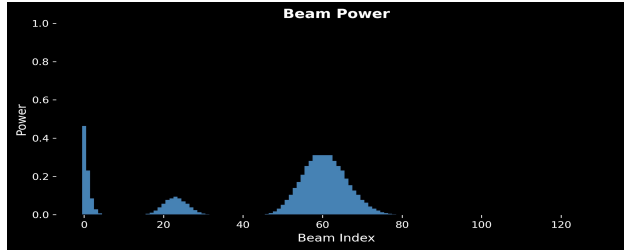
(a) RGB Image



(b) Depth Image



(c) Location Information



(d) Beam Power

Fig. 5: (a)–(d) respectively illustrate the depth map, RGB image, CSI beam visualization, and the corresponding 3D spatial coordinates, where blue markers indicate the UAV position and orange markers denote the base station location.

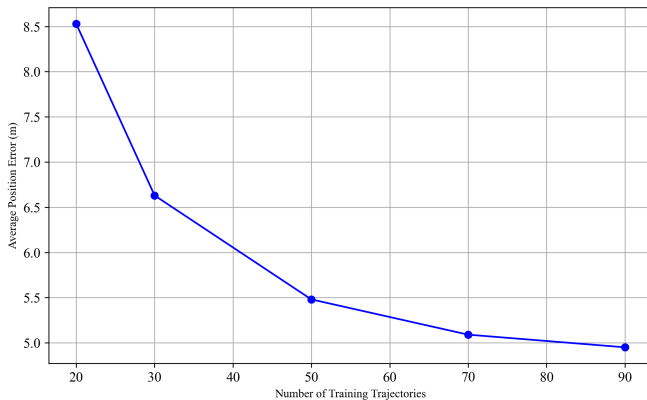


Fig. 6: Relationship between the number of training trajectories and average positioning error.

TABLE II: Comparison of Generalization Performance Between Great-MSD and Sionna RT.

Train	Test	Average (m)
Sionna RT-trian	SionnaRT-test	0.309
Great-MCD-trian	Great-MSD-test	0.647
Sionna RT-trian	Great-MSD-test	11.082
Great-MCD-trian	SionnaRT-test	8.107

limited generalization ability when transferred to the Great-MSD, with an average positioning error of 11.082 meters. Nevertheless, on its native platform, this model performs exceptionally well, achieving an average error of just 0.309

meters on unseen trajectories, reflecting its overfitting.

To assess and visualize the differences between the simulation platforms, we apply a two-dimensional fast Fourier transform (2D FFT) to CSI, thereby obtaining the angle-delay profile (ADP). As illustrated in Fig 7, both simulation platforms demonstrate high consistency in the line-of-sight (LOS) components. This alignment supports the observed generalization capability between the platforms, indicating that core propagation mechanisms are accurately captured by both simulators.

In contrast, notable discrepancies are evident in the non-line-of-sight (NLOS) components. Great-X employs an Unreal Engine-based renderer, which provides higher geometric precision and more detailed texture information than Sionna RT’s Mitsuba renderer implementation. This difference in rendering fidelity translates into improved accuracy in modeling complex multipath interactions within NLOS propagation paths. Specifically, Great-X’s ray-tracing algorithms are better equipped to capture the intricate scattering and reflection patterns that characterize NLOS signal propagation.

The observed agreement in LOS characteristics across both platforms confirms that fundamental wave propagation phenomena are consistently modeled. However, the divergence in NLOS behavior highlights the architectural advantages of Great-X’s Unreal Engine-based rendering pipeline, underscoring its potential for more realistic and detailed channel modeling in complex environments, making it particularly suitable for 6G channel modeling requirements.

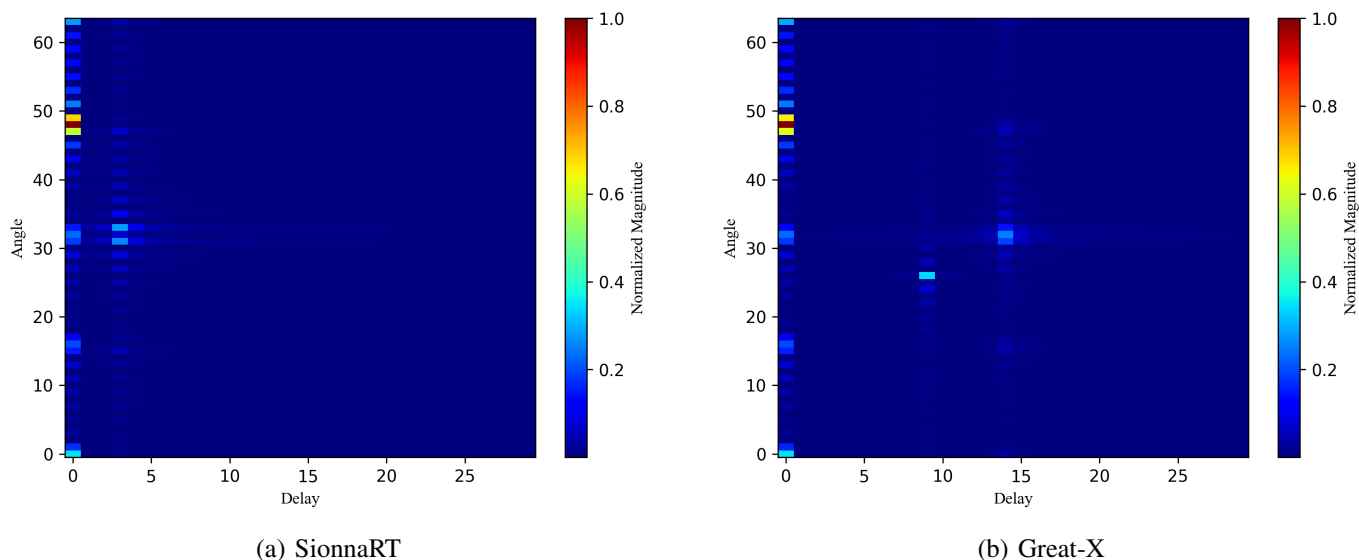


Fig. 7: Comparison of ADPs from different simulators: (a) for SionnaRT, and (b) for Great-X.

## V. CONCLUSIONS

This paper introduces Great-X, the pioneering unified open-source simulation platform designed for multimodal perception. It enables synchronous simulation of optical and wireless channel data within a single engine. Great-X leverages Unreal Engine to reconstruct the electromagnetic process of channel simulation based on ray tracing, significantly enhancing simulation speed while maintaining high accuracy. By integrating these functionalities into a cohesive framework, Great-X provides an unprecedented infrastructure for developing and validating advanced multimodal sensing algorithms.

Building upon the capabilities of Great-X, we have developed Great-MSD, a novel multimodal UAV position simulation dataset specifically tailored for low-altitude scenarios. Great-MSD includes comprehensive data from cameras, CSI, and accurate spatial coordinates, providing a rich resource for training and evaluating models in complex environments.

We plan to continuously expand the Great-X platform by incorporating more diverse environmental layouts, obstacle distributions, and dynamic behaviors. These efforts will contribute to developing integrated perception systems with enhanced realism, stability, and applicability.

## REFERENCES

- [1] L. Alzubaidi, J. Bai, A. Al-Sabaawi, J. Santamaría, A. S. Albahri, B. S. N. Al-Dabbagh, M. A. Fadhel, M. Manoufali, J. Zhang, A. H. Al-Timemy *et al.*, “A survey on deep learning tools dealing with data scarcity: definitions, challenges, solutions, tips, and applications,” *Journal of Big Data*, vol. 10, no. 1, p. 46, 2023.
- [2] Y. Gao, H. Hu, J. Zhang, Y. Jin, S. Xu, and X. Chu, “On the performance of an integrated communication and localization system: an analytical framework,” *IEEE Transactions on Vehicular Technology*, vol. 73, no. 7, pp. 10 845–10 849, 2024.
- [3] Y. Gao, H. Du, Z. Jiang, H. Hu, J. Zhang, S. Zhang, J. Du, F. R. Yu, and S. Xu, “A stochastic geometry-based analytical framework for integrated localization and communication systems,” *IEEE Internet of Things Journal*, 2025.
- [4] Y. Gao, X. Xu, Y. Jin, W. Yuan, J. Zhang, and S. Xu, “Joint channel estimation and data detection for ofds systems: A lightweight deep learning framework with a novel data augmentation method,” *IEEE Internet of Things Journal*, 2025.
- [5] Y. Tian, Q. Zhao, F. Boukhalfa, K. Wu, F. Bader *et al.*, “Multimodal transformers for wireless communications: A case study in beam prediction,” *arXiv preprint arXiv:2309.11811*, 2023.
- [6] A. Alkhateeb, “Deepmimo: A generic deep learning dataset for millimeter wave and massive mimo applications,” *arXiv preprint arXiv:1902.06435*, 2019.
- [7] Wireless insite propagation modeling software. [Online]. Available: <https://www.remcom.com/wireless-insite-propagation-software>
- [8] U. Demirhan, A. Taha, S. Jiang, and A. Alkhateeb, “DeepVerse 6G: A dataset generation framework for multi-modal sensing and communication digital twins,” *preprint*, Feb 2025.
- [9] A. Dosovitskiy, G. Ros, F. Codevilla, A. Lopez, and V. Koltun, “Carla: An open urban driving simulator,” in *Conference on robot learning*. PMLR, 2017, pp. 1–16.
- [10] X. Cheng, Z. Huang, Y. Yu, L. Bai, M. Sun, Z. Han, R. Zhang, and S. Li, “Synthsom: A synthetic intelligent multi-modal sensing-communication dataset for synesthesia of machines (som),” *Scientific Data*, vol. 12, 2025.
- [11] Remcom Inc. Wavefarer automotive radar simulation software. [Online]. Available: <https://www.remcom.com/wavefarer-automotive-radar-software>
- [12] S. Shah, D. Dey, C. Lovett, and A. Kapoor, “Airsim: High-fidelity visual and physical simulation for autonomous vehicles,” in *Field and Service Robotics: Results of the 11th International Conference*. Springer, 2018, pp. 621–635.
- [13] Sionna. [Online]. Available: <https://nvlabs.github.io/sionna/rt>
- [14] ITU, “Recommendation itu-r p.2040-3: Effects of building materials and structures on radiowave propagation above about 100 mhz,” International Telecommunication Union, Tech. Rep., Sep. 2023, series P.
- [15] Epic Games. Unreal engine official website. [Online]. Available: <https://www.unrealengine.com>
- [16] K. He, X. Zhang, S. Ren, and J. Sun, “Deep residual learning for image recognition,” in *Proceedings of the IEEE conference on computer vision and pattern recognition*, 2016, pp. 770–778.